A Melting Layer Model for Passive/Active Microwave Remote Sensing Applications- Part II: Simulation of TRMM Observations

William S. Olson[1], Peter Bauer[2], Christian D. Kummerow[3], Ye Hong[4], and Wei-Kuo Tao[3]

[1]JCET, University of Maryland Baltimore County

[2]Deutsche Forschungsanstalt fuer Luft- und Raumfahrt

[3]Laboratory for Atmospheres, NASA/Goddard Space Flight

[4]Caelum Research Corporation, Inc.

to be submitted to the *Journal of Applied Meteorology*

January 4, 2000

Abstract

The one-dimensional, steady-state melting layer model developed in Part I of this study is used to calculate both the microphysical and radiative properties of melting precipitation, based upon the computed concentrations of snow and graupel just above the freezing level at applicable horizontal gridpoints of 3-dimensional cloud resolving model simulations. The modified 3-dimensional distributions of precipitation properties serve as input to radiative transfer calculations of upwelling radiances and radar extinction/reflectivities at the TRMM Microwave Imager (TMI) and Precipitation Radar (PR) frequencies, respectively.

At the resolution of the cloud resolving model grids (~1 km), upwelling radiances generally increase if mixed-phase precipitation is included in the model atmosphere. The magnitude of the increase depends upon the optical thickness of the cloud and precipitation, as well as the scattering characteristics of ice-phase precipitation aloft. Over the set of cloud resolving model simulations utilized in this study, maximum radiance increases of 43, 28, 18, and 10 K are simulated at 10.65, 19.35 GHz, 37.0, and 85.5 GHz, respectively. The impact of melting on *TMI-measured* radiances is determined not only by the physics of the melting particles but also by the horizontal extent of the melting precipitation, since the lower-frequency channels have footprints that extend over 10's of kilometers. At TMI resolution, the maximum radiance increases are 16, 15, 12, and 9 K at the same frequencies.

Simulated PR extinction and reflectivities in the melting layer can increase dramatically if mixed-phase precipitation is included, a result consistent with previous studies. Maximum increases of 0.46 (-2 dB) in extinction optical depth and 5 dBZ in reflectivity are simulated based upon the set of cloud resolving model simulations.

1. Introduction

In Part I, a physical model that describes the melting of ice-phase precipitation within the stratiform regions of "parent" 3-D cloud resolving model (CRM) simulations was presented. Alternative methods for calculating the dielectric and radiative properties of melting precipitation were compared, and the optical depths and reflectivities of the simulated melting layer were compared to observations. Here, the parent 3-D CRM fields that have been modified to include melting precipitation serve as the basis for simulations of upwelling microwave radiances and extinction/reflectivities as they might be measured by the Tropical Rainfall Measuring Mission (TRMM) Microwave Imager (TMI) and Precipitation Radar (PR) instruments, respectively.

The parent 3-D CRM simulations, described in Part I, all provide fields of temperature, pressure, humidity, cloud and precipitation on Cartesian grids. Table 1 of Part I summarizes the basic characteristics of the parent simulations. The three Goddard Cumulus Ensemble (GCE) model runs simulate the development of tropical mesoscale convective systems over the ocean. A thunderstorm complex over land and a hurricane simulation are derived from the University of Wisconsin Non-hydrostatic Modeling System (UW-NMS) model runs. At each gridpoint classified as stratiform in these parent simulations, the one-dimensional melting model is initialized using the ice precipitation distributions (snow and graupel) at the parent model level just above the freezing level.

The current TMI operational precipitation algorithm at the TRMM Science Data and Information System is based upon a Bayesian estimation technique, which draws upon a database of simulated CRM profiles to construct retrieved precipitation profiles. For each model profile in the database, an upwelling radiance is calculated based upon radiative transfer theory. Then, given a set of TMI-observed radiances, a retrieved profile (including precipitation species and latent heating rates) is constructed from those model profiles in the database that are radiatively consistent with the observations; i.e., those model profiles associated with calculated radiances similar to the observed radiances. It follows that a bias in the calculated radiances will lead to errors in the retrieved profiles. Since the presence of mixed-phase, partially melted precipitation can significantly increase the radiative absorption and scattering within the stratiform regions of a mesoscale convective system (ref. Part I), a neglect of mixed-phase precipitation could lead to significant errors in retrieved rain rates and precipitation/latent heating profiles. Similarly, the presence of melting precipitation can lead to increases in radiative extinction and radar reflectivity just below the freezing level; therefore errors in the interpretation of PR observations could also result from the omission of mixed-phase precipitation.

The objective of this study is to quantify the changes in simulated upwelling microwave radiances at the TMI frequencies and extinction/radar reflectivities at the PR frequency due to the explicit modeling of melting precipitation. These radiative simulations include not only the calculation of the transfer of radiation through the model atmospheres but also the specific representation of antenna patterns and sampling geometry of the instruments. For reference, the TMI and PR instrument characteristics are included in Table 1. This work follows the efforts of Schols et al. (1997), and Bauer et al. (1999a,b), who simulated radiances upwelling from model atmospheres that included melting hydrometeors. The present study differs from previous work in that a more complete model of the melting process, including particle interactions, is utilized, and the dielectric properties of melting snow are calculated using a more realistic approach (see Part I). Also, since the radiative calculations are performed based upon three-dimensional CRM simulations, the effects of melting within spatially extensive radiometer footprints can be examined.

2. Simulation of TMI Radiances

a. Sensor Component

The first step in simulating TMI radiances is to compute the upwelling radiances along prescribed paths through each parent 3-D CRM domain. The radiance paths are determined by the viewing geometry of the TMI. The TMI scans conically at a constant off-nadir angle of 49°, resulting in a boresight incidence angle of 52.7° from zenith at the earth's surface. TMI observations are also diffraction-limited, such that the maximum response of the instrument is along the boresight but generally falls off with angular displacement from the boresight. The angular response function, or antenna pattern, decreases to half the maximum response at an off-boresight angle of $\Lambda/2$, where Λ is defined as the beamwidth of the pattern. At the earth's surface, the half-maximum of the antenna pattern prescribes an ellipse called the sensor footprint. Due to diffraction effects and the fixed aperture size of the TMI, the beamwidths and footprint dimensions of the TMI antenna patterns decrease with increasing channel frequency; see Table 1.

In the present study, the antenna patterns of the TMI are approximated using analytical functions that closely fit the specifications of the actual antenna patterns. The TMI patterns are modeled as two-dimensional Gaussian functions that have the same half-maximum widths as the actual patterns. The fit patterns are then spatially convolved over the small displacement of the sensor view during the measurement integration period (3.1 ms at 85.5 GHz; 6.4 ms at the other TMI frequencies). Each convolved pattern is then discretized into small elements of solid angle, for which the mean response is computed.

The geometry of a TMI measurement is depicted in Fig. 1. The antenna pattern is defined in the coordinate system with axes x', y', and z' (the antenna boresight direction). The mean antenna response per unit solid angle at polar coordinates θ, ϕ is given by $g[\theta,\phi]$. Simulated TMI radiance measurements, or brightness temperatures, are calculated by a numerical integration of the upwelling radiance field over the antenna response pattern,

$$TB_{v,p} = \frac{1}{G_v} \sum_{i,j} \hat{g}_v[\theta_i, \phi_j] \, TB^*_{v,p}[\theta_i, \phi_j] \, \Delta\Omega_{ij}, \tag{1}$$

where

$$G_v = \sum_{i,j} \hat{g}_v[\theta_i, \phi_j] \, \Delta\Omega_{ij}, \tag{2}$$

and

$$\Delta\Omega_{ij} = \left(\cos(\theta_i - \Delta\theta/2) - \cos(\theta_i + \Delta\theta/2)\right) \Delta\phi. \tag{3}$$

Here, $\hat{g}$ is the average antenna response over the incremental solid angle $\Delta\Omega_{ij}$, which is bounded by the angles $\theta_i - \Delta\theta/2$, $\theta_i + \Delta\theta/2$, and $\phi_j - \Delta\phi/2$, $\phi_j + \Delta\phi/2$. The angles θ_i and ϕ_j define a vector relative to the antenna boresight for each solid angle increment. Given the altitude of the TRMM observatory (350 km) and scan geometry of the TMI, the vector defined by θ_i and ϕ_j can be scaled to define a path through the earth's atmosphere to the surface. The upwelling microwave radiance along this path is $TB^*_{v,p}$, where ν and p are frequency and polarization indices, respectively. The path of the incoming radiance that contributes to $TB^{*}_{v,p}$ by reflection off the earth's surface is also determined assuming specular reflection (see Fig. 1). The summations in (1) and (2) are carried out to an angle θ of 1.25 Λ, with increments of $\Delta\theta$ (0.095°) and $\Delta\phi$ (2° to 24°; increasing with channel frequency) that provide a good representation of the integrals, given the resolution of the parent model grids. TMI radiances are simulated for scan position 105, which is close to the sub-satellite track.

In the present study, each CRM domain is placed on the earth's surface such that the x coordinate of the domain is eastward and the y coordinate is northward. Atmospheric properties from the CRM at each gridpoint are interpolated in the vertical to standard levels with 0.5 km spacing below 10 km and 1.0 km spacing above, up to 18 km. The path of each upwelling radiance is traced through the CRM domain, and atmospheric properties from the CRM simulation are sampled from the gridpoint nearest to the radiance path at each standard grid-level (see Fig. 1). The CRM domain is assumed to repeat periodically over the earth's surface, such that radiance paths which fall outside the original model domain will instead pass through one of the repeated domains. In this situation, atmospheric properties along the radiance path can be sampled from the repeated domain.

b. Radiative Transfer Component

The properties of the atmosphere, sampled from the parent 3-D CRM simulations, are used to calculate the microwave radiative properties at the TMI frequencies along each radiance path. Radiative absorption by molecular oxygen and water vapor in the atmosphere are determined from the sampled temperature, pressure, and relative humidity according to the model of Liebe (1985). The size distribution of liquid cloud drops is assumed to follow a gamma distribution as in Liou (1992) with a 6 μm mode radius and a water content given by the parent simulation. It is assumed that cloud ice particles have a size distribution described by the empirical formulae of Heymsfield and Platt (1984), given the temperature and ice equivalent water content derived from the parent simulation. The radiative properties (extinction coefficient, single scatter albedo, and asymmetry factor) of cloud liquid and ice are determined from Mie theory (Mie, 1908), which assumes spherical, homogeneous particles. In applications to cloud ice particles, ice spheres with the same equivalent water content as the crystals are specified. Liquid and ice precipitation water contents and size distributions are derived directly from the parent simulation except in stratiform regions where the melting model is applied. The radiative properties of rain and non-melting ice precipitation are again calculated from Mie theory. The refractive indices of snow and graupel particles, which contain ice and air, are computed using Maxwell-Garnett (1904) dielectric mixing for air inclusions within an ice matrix; see (45) and (46) of Part I.

In stratiform regions where the one-dimension melting model is applied, the water contents and radiative properties of the mixed-phase melting precipitation particles are substituted at all standard levels of the parent simulation between the freezing level and 3 km below the freezing level (the extent of the melting model domain). Rain water contents from the melting model are also substituted for the rain water contents of the parent simulation, but the drop-size distribution of rain is assumed to be the same as in the parent simulation, and the radiative properties of rain are calculated using Mie theory. Calculation of the radiative properties of mixed-phase, melting particles is described in Part I, and applications of specific dielectric/radiative property models to the microwave radiance simulations that follow are indicated.

Radiative transfer simulations in this study are limited to atmospheres overlying water-surface backgrounds. Over these backgrounds the effects of microwave absorption by the melting layer are expected to be most significant. The model of Wilheit (1979) is utilized to describe the dependence of water surface emissivity/reflectivity on wind speed. Simulations assuming 20-meter wind speeds of 0, 6, 12, and 18 m s^{-1} are performed, and specular reflection off the water surface is assumed. The isotropic, downwelling cosmic background radiance (2.7 K) at the top of the model atmosphere is also included.

Once the surface conditions and radiative properties of the atmosphere along a given radiance path are specified, a radiative transfer calculation of $TB^{*}_{\nu p}$ is performed. The radiative transfer method is based upon Eddington's second approximation (ref. Weinman and Davies 1978; Robinson et al. 1992), but with a modification to account for the oblique radiance path through the three-dimensional CRM domain (Olson and Kummerow, 1996; Bauer et al. 1998). Here, Eddington's second approximation is applied independently to the two "slanted" profiles of atmospheric constituents defined by the incoming (downwelling) and outgoing (upwelling) radiance paths. The application of the method to the downwelling radiance path yields the downwelling radiance at the earth's surface, from which the reflected portion of the radiance can be calculated. The method is then re-applied to the upwelling radiance path, incorporating the reflected radiance as part of the surface boundary condition. The upwelling radiance at the top of the atmosphere, $TB^{*}_{\nu p}$, is calculated in this step.

The accuracy of the slant-path Eddington (hereafter SPE) approximation is illustrated using the TOGA1 CRM simulation at 180 minutes (see Part I, Table 1), for which the effects of melting are not included. Displayed in Fig. 2a and b are plan views of the vertically-integrated precipitating liquid and ice hydrometeors from the CRM. In Fig. 2c and d are the fields of radiances at model grid-resolution at 19.35 and 85.5 GHz, calculated using SPE. Grid resolution is achieved by substituting a delta function response along the antenna boresight for the TMI response function ˆg. Equation (1) is then applied, such that the antenna boresight of the sensor intersects the earth's surface at each model gridpoint, successively, creating a field of radiances/reflectivities at the horizontal resolution of the CRM grid (1 km). The TMI radiance path is assumed to lie parallel to the bounding *y*-*z* plane of the CRM model domain, with the sensor viewing toward the north (+*y*) at the boresight incidence angle (52.7°). For comparison, radiances are also calculated using a rigorous Monte Carlo (hereafter MC) method, as described by Roberti et al. (1994). The MC calculated radiances appear in Fig. 2e and f at 19.35 and 85.5 GHz, respectively.

Note that the plan views of radiances from the SPE and MC methods appear very similar in pattern and magnitude. Radiance differences at 5 km resolution at four of the TMI channel frequencies are plotted as functions of the SPE radiances in Fig. 3. Five km resolution corresponds to the maximum resolution of the TMI. At 10.65, 19.35, and 37.0 GHz, errors in SPE radiances are mostly less than 10 K, with error standard deviations in raining areas of 2.2, 2.0, and 3.3 K, respectively. At 85.5 GHz, some relatively large underestimates of the radiances occur, and the error standard deviation is greater (4.3 K). The underestimates correspond to regions near the leading edge of strong scattering maxima (low radiances), where relatively high-intensity thermal emission from outside the cloud is scattered towards the sensor in the MC approach, but not in SPE. Errors of this magnitude at 85.5 GHz were previously obtained by Kummerow et al. (1996; Fig. 2) in the strong scattering region of a simulated squall line. In sum, radiance calculations at 85.5 GHz using SPE in strong scattering regions must be regarded with caution. However, since the goal of the present study is to determine the differential effect of melting precipitation on upwelling microwave radiances, the SPE approximation is adequate.

3. Simulation of PR Reflectivities

a. Sensor Component

The PR antenna is a 2 m x 2 m rectangular array with a beamwidth of 0.71° in both the along-track and cross-track directions at nadir view. The instrument scans electronically ±17° cross-track, but simulations in the present study are limited to nadir-view. The diffraction limitation of the PR is modeled in a manner analogous to the TMI. The PR two-way gain function, $h[\theta,\phi]$, is approximated by the square of the diffraction pattern of a square aperture. The aperture dimension is scaled such that the half-maximum width of the diffraction pattern is equal to the PR beamwidth. The effective reflectivity of a PR measurement at range r is then given by

$$Z[r] = \frac{1}{H}\sum_{i,j} \hat{h}\left[\theta_i,\phi_j\right] Z^{*}\left[\theta_i,\phi_j,r\right] \Delta\Omega_{ij}, \tag{4}$$

where

$$H = \sum_{i,j} \hat{h}\left[\theta_i,\phi_j\right] \Delta\Omega_{ij}. \tag{5}$$

Here, $\hat{h}$ is the average two-way gain function of the PR over $\Delta\Omega_{ij}$ in the direction defined by θ_i, ϕ_j relative to the antenna boresight (see Fig. 1), and $Z*$ is the path-attenuated reflectivity along the same direction, corresponding to the range bin between $r - \Delta r/2$and $r + \Delta r/2$. The PR range resolution, Δr, is 250 m. The numerical integrals (4) and (5) are evaluated out to an angle θ equal to 1.25 Λ, using angular increments $\Delta\theta$ and $\Delta\phi$ equal to 0.225° and 36°, respectively.

b. Extinction and Reflectivity Calculations

The radiative properties of the atmospheric constituents at each horizontal gridpoint in the CRM simulation, interpolated to the standard vertical levels (see Section 2b), are sampled along the PR radiance paths defined by θ_i, ϕ_j. The effective reflectivity of the range bin at range r along a given path is

$$Z^* = \frac{c^4}{4\pi^6 \nu^4 |K_l|^2} \left\{ \overline{k_{ext}(r)\omega_o(r) P_{180}(r)} \right\} \exp\left[-2 \sum_m \overline{k_{ext}(r')}_m \, \Delta r'_m \right]. \qquad (6)$$

Here, c is the speed of light in a vacuum, ν is the operating frequency of the radar (13.8 GHz), and $|K_l|^2$ is a liquid water dielectric factor that has a value of 0.93. The parameters k_{ext}, ω_o, and P_{180}, are the extinction coefficient, single scatter albedo, and backscatter phase function of the atmosphere, respectively. The product of these three parameters is the backscatter cross section of the atmosphere, and the overbar indicates a spatial average of the cross section between $r - \Delta r/2$ and $r + \Delta r/2$ along the radiance path. The exponential term represents the two-way attenuation of the reflectivity; the summation in rectangular brackets is over all reflectivity bins from the top of the CRM domain to the range r. Note that the thermal noise power is not included in the present simulation of Z^*, but may be added as a second term on the right-hand side of (6); see Olson et al. (1996).

The calculation of the radiative properties of the model atmosphere is based upon the methods described in Section 2b but for a frequency of 13.8 GHz; i.e., the TMI and PR calculations are consistent.

4. Squall Line Radiance/Reflectivity Simulations Including Melting

The TOGA1 CRM run at 180 minutes is again selected to demonstrate the radiance and reflectivity simulations. Distributions of partially-melted ice precipitation are included in the simulations by applying the one-dimensional melting model in stratiform areas, assuming the FS core-shell dielectric model for melting snow and the MGwi dielectric model for melting graupel; ref. Part I of this series for a complete description.

Before considering the effects of sensor resolution, it is instructive to analyze the radiance and reflectivity fields simulated at the highest possible resolution. Grid-resolution radiance/reflectivity fields are obtained by substituting a delta function response along the antenna boresight for both the TMI and PR response functions ^g and

ˆh, respectively. Equations (1) and (4) are then applied, such that the antenna boresight of the sensors intersect the earth's surface at each model gridpoint, successively, creating a field of radiances/reflectivities at the horizontal resolution of the CRM grid (1 km). The TMI radiance paths are assumed to lie parallel to the bounding *y*-*z* plane of the CRM model domain, with the sensor viewing toward the north (+*y*). The PR always views toward nadir (-*z*) in the simulation.

Presented in Fig. 4 are plan views of the simulated radiance fields at the TMI frequencies, corresponding to the liquid and ice precipitation distributions shown in Fig. 2a and b. Note that there is a strong correlation between concentrations of liquid precipitation and higher radiances at the 10.65, 19.35, and 37 GHz frequencies. Convective rain, located primarily along the eastern and southern edges of the simulated squall line, produces relatively strong microwave emission at these frequencies. Stratiform rain to the north and west of the convection tends to produce less emission, although the difference between convective and stratiform rain emission decreases with increasing frequency. At 85.5 GHz, greater microwave emission from the water surface background and atmospheric water vapor in rain-free regions is essentially indistinguishable from rain emission. However, precipitation-sized ice particles (snow and graupel) scatter microwaves and create depressions in the upwelling radiance field. The deepest convective cells, seen along *x*=50, generally produce the most ice-scattering and therefore the lowest radiances, while shallower cells along the eastern and southern edges of the squall line are associated with less ice and relatively weak scattering. Stratiform regions, such as the area near x=40, y=80, may also exhibit significant scattering depressions. Finally, note the relatively high radiances (>280 K) along the southern edge of the squall line at 19.35, 37, and 85.5 GHz. These high radiances are caused by downwelling emission from cloud and precipitation that is reflected off the water surface toward the sensor, an effect described previously by Petty (1994).

Since the effects of melting precipitation are not obvious in plots of total radiance, the differences between the simulated radiance fields of Fig. 4 and those produced by a simulation without mixed-phase precipitation are presented in Fig. 5. In general, radiances at the TMI frequencies increase with melting. Along the transect x =50 km at 10.65 GHz, for example, a train of decaying convective cells produces patches where radiances increase by more than 18 K. The more "stratiform" melting region near x=40 km, y =80 km, yields radiances that increase by 6 to 10 K relative to the control simulation. The general increase of radiances at 10.65 GHz is attributed to the increase of radiative absorption/emission due to the presence of mixed-phase, melting precipitation; ref. Part I, Section 2.

As the frequency increases from 10.65 GHz to 19.35 and then to 37 GHz, some of the regions of enhanced radiances persist, while other appear to decay. For example, increased emission at 19.35 and 37 GHz is associated with most of the decaying convective cells along x = 50 km. However, near x=50 km, y=80 km, the region of enhanced emission at 10.65 GHz nearly disappears at 19.35 GHz, and radiances actually decrease with melting at 37 GHz.

The frequency-dependence of the radiances near x=50 km, y=80 km is determined by the precipitation geometry and melting particle absorption, which generally increases with frequency. Located near the point in question is an active convective cell with a relatively high rain water at content at low levels (Fig. 2a), and long the oblique radiance path between the cell and the sensor is a region of melting precipitation. At 10.65 GHz, total absorption and emission by the cell and melting layer is relatively weak, and so the upwelling radiance increases with the addition of mixed-phase precipitation in the melting layer (Fig. 5a). At 19.35 GHz, absorption/emission by the cell is stronger and the additional emission produced by the melting precipitation produces a smaller increase in the upwelling radiance (Fig. 5b). At 37 GHz the absorption/emission by the cell is very strong, and the effective brightness temperature of the cell is close to the atmospheric temperature at low levels (~280 K). These relatively intense radiances are partially absorbed by the melting layer, which emits at a characteristic temperature of only 273 K, thereby reducing the upwelling radiance at the top of the atmosphere (Fig. 5c).

At 85.5 GHz, the effects of melting precipitation are generally more subtle in comparison to the lower frequencies (Fig. 5d). Even though absorption/emission by melting precipitation is greatest at 85.5 GHz, scattering by ice precipitation aloft tends to mask the enhanced emission regions. Notwithstanding, enhanced emission from melting precipitation near x=50 km, y=40 km, and x=50 km, y=90 km is not obscured by overlying snow and graupel, and radiance increases greater than 14 K are seen. In the broad stratiform region near x=40 km, y=80 km, more modest increases on the order of 4 K are noted. Elsewhere, both increases and decreases of radiances due to melting precipitation are relatively small.

Presented in Fig. 6 are simulations of radiative extinction, k_{ext}, and path-attenuated radar reflectivity, Z, at the PR frequency in a vertical cross-section of the TOGA1 model domain at y=75 km (see Fig. 2a,b for reference). The cross section passes through a broad area of stratiform rain between x=30 km and x=70 km, corresponding to ice precipitation equivalent water contents greater than 0.2 g m^{-3} just above the freezing level. Both the simulated radiative extinction and radar reflectivities exhibit maxima near 5 km altitude, or about 0.6 km below the freezing level. The extinction and melting-layer reflectivities are greatest between x=30 km and x=50 km in the cross section, resulting from the seeding of the melting layer by higher equivalent water contents of graupel. Between x=50 km and x=70 km, the melting layer is mainly seeded by snow, which melts faster and produces weaker extinction and lower reflectivities. Note that the presence of mixed-phase precipitation accounts for almost all of the extinction and about a 5 dBZ increase in reflectivities in the melting layer; Fig. 6e, f. Also, due to attenuation of radar transmitted power within the melting layer, there is a slight decrease in rain reflectivities below the melting layer.

Now the effects of sensor resolution are included in the simulations using the approximate response functions $\hat{g}$ for TMI and $\hat{h}$ for PR in (1) and (4), respectively. The radiance and reflectivity calculations with and without mixed-phase precipitation are repeated, and the difference fields are presented in Fig. 7.

Although melting leads to increases greater than 18 K in grid-resolution radiances at 10.65 and 19.35 GHz, the relatively low resolution of these TMI channels (footprint dimensions roughly 40 km and 20 km, respectively) limits the "measured" increases to about 5 K at 10.65 GHz and 7 K at 19.35 GHz. The scale of the melting regions in the TOGA1 simulation also has an impact on the radiance increases. The decaying convective cells seen in Fig. 5 along x=50 km produce the greatest increases in upwelling radiances at high resolution, but these patches have dimensions ~10 km, which is smaller than the footprint dimensions at 10.65 and 19.35 GHz. The stratiform precipitation near x=40 km, y=80 km produces a smaller increase in radiances at grid resolution, but it covers an area of roughly 20 km x 30 km. Therefore, the stratiform rain area makes a comparable contribution to the overall increase of radiances at sensor resolution. In the tropics, stratiform precipitation regions may extend 100 km or more in organized mesoscale convective systems (ref. Rickenbach and Rutledge, 1998), and in these situations, greater radiance increases could be observed at 10.65 and 19.35 GHz. At 37 GHz, sensor resolution effects are less severe (footprint dimension of roughly 10 km), and radiance increases greater than 6 K are seen over a much larger area than at 19.35

GHz. The 85.5 GHz channels of the TMI have the best resolution (footprint ~5 km), but the effects of ice scattering offset the potential increases in emission due to melting. Increases less than 2 K are indicated over most of the extent of the squall line at 85.5 GHz.

The PR has relatively high resolution at nadir view (4.3 km footprint) and the increases in extinction and reflectivity in the melting layer are almost fully realized at sensor resolution.

5. General Impact of Melting on TMI and PR Simulations

Radiative simulations based upon all of the CRM runs (see Part I, Table 1) are performed for TMI and PR, both at grid resolution and with the instrument response functions applied. Each radiative simulation is performed (a) assuming no mixed-phase particles (meltwater is assumed frozen until the particle is completely melted), (b) assuming the FS core-shell dielectric model for melting snow and the MGwi dielectric model for melting graupel, and (c) assuming the FS core-shell model for snow and the ML97 model for graupel.

a. Impact of Melting on TMI Radiances

The impact of mixed-phase, melting precipitation on upwelling radiances at the TMI frequencies can be approximately described by a simple radiative model. First, from (1) it is assumed that the integrated response of TMI over the region of melting precipitation is given by f_{mb}, such that

$$TB_{v,p} = f_{mb}\, TB^{*}_{mb\, v,p} + \left(1 - f_{mb}\right) TB^{*}_{fov\, v,p}, \tag{7}$$

where $TB^{*}_{mb\ v,p}$ is the average radiance upwelling from the melting region, and $TB^{*}_{fov\ v,p}$ is the average radiance within the sensor field of view if no accounting for the effects of mixed-phase particles is taken. By this definition, the change in the total radiance, $TB_{v,p}$, due to the presence of melting particles is

$$\Delta TB_{v,p} = f_{mb}\left(TB^{*}_{mb\, v,p} - TB^{*}_{fov\, v,p}\right). \tag{8}$$

It is further assumed that the earth's surface is characterized by a surface temperature T_s and a reflectivity r_s, and that the entire atmosphere is represented by a single layer with a temperature T_{atm}, and a transmittance Π_{atm}. Under these assumptions the radiance upwelling from a specific region can be approximated by

$$TB^{*} \approx T_s \left(1 - r_s\right) \Pi_{atm} + T_{atm}\left(1 - \Pi_{atm}\right)\left(1 + r_s\, \Pi_{atm}\right). \tag{9}$$

Here, the effects of scattering, as well as the small radiative contribution from the cosmic background, are ignored. A final simplification, $T_s \approx T_{atm}$, reduces (9) to

$$TB^{*} \approx T_{atm}\left(1 - r_s\,\Pi^2_{atm}\right). \tag{10}$$

Expression (10) can be applied to the radiances on the right-hand side of (8) by noting that the total transmittance of the atmosphere, Π_{atm}, is equal to Π_{fov} outside the melting region and $\Pi_{fov} \bullet \Pi_{mb}$ inside the melting region. Substituting these transmittances successively into (10) and then substituting the resulting expressions into (8) leads to the following relation for the change of the total radiance due to melting.

$$\Delta TB_{v,p} = f_{mb}\left(T_{atm} - TB_{fov\,v,p}\right)\left(1 - \Pi^2_{mb}\right). \tag{11}$$

Here, $TB_{fov\ v,p}$ is the total radiance if no mixed-phase precipitation is considered. From (11), the impact of melting relative to a simulation which does not explicitly include mixed-phase precipitation is primarily a function of the fractional coverage of melting precipitation within the sensor field of view and the transmittance of the melting layer. The impact is modulated, however, by the difference between the atmospheric temperature and the upwelling radiance in the absence of mixed-phase particles.

Using (11) as a guide, radiance differences at grid resolution due to melting are plotted versus the difference $T_{atm} - TB_{fov\ v,p}$ in Fig. 8, with T_{atm} set to 273 K. Only radiances emanating from 10 km x 10 km model regions with all gridpoints classified as "stratiform" (see Part I, Section 2a) are selected in order to isolate the impact of melting on atmospheric transmittance (i.e., $f_{mb} \approx 1$). Isolines of melting layer optical depth from 0 to 0.2 based upon (11) are overlaid in the Figure.

The inclusion of the FS snow/MGwi graupel melting layer clearly increases the optical depth of the precipitation layer at 10.65, 19.35, and 37 GHz, as seen in Fig. 8a, c, and e, respectively. Even though the optical depths of the melting layers generally increase with frequency, the greatest increases in the upwelling radiances occur at 10.65 GHz, with more modest increases at 19.35 GHz, and even smaller increases at 37 GHz. Maximum increases of 43 K, 28 K, and 18 K due to melting are attained at 10.65, 19.35, and 37 GHz, respectively. The frequency-dependence of the maxima is linked to the general decrease of $T_{atm} - TB_{fov\ v,p}$ with frequency. At 85.5 GHz, the simple model represented by (11), above, breaks down because radiative scattering is the dominant process at this frequency (Fig. 8g). The FS snow/ML97 graupel melting layers have generally lower optical depths and produce smaller increases in upwelling radiances; see Fig. 8b, d, and f. The maximum radiance increases due to melting are about 32 K, 20 K, and 15 K at 10.65, 19.35, and 37 GHz, respectively.

The plots of Fig. 8 are repeated in Fig. 9, substituting the simulated radiances at TMI resolution. The maximum radiance increases due to the FS snow/MGwi graupel melting layer are16 K, 15 K, and 12 K at 10.65, 19.35, and 37 GHz, respectively; see Fig. 9a, c, and e. These increases are approximately 37%, 54%, and 67% of the increases at grid resolution, a result that can be explained by the spatial averaging effect of the sensor response functions: the greatest spatial averaging occurs at 10.65 GHz, and decreases with increasing frequency. The maximum radiance increase due to melting at 85.5 GHz is 9 K (Fig. 9g), which is about the same as the increase at grid resolution. The FS snow/ML97 graupel melting layers yield radiance increases at sensor resolution that are similarly reduced.

b. Impact of Melting on PR Reflectivities

Plotted in Fig. 10 are the simulated extinction optical depth and mean reflectivity differences due to mixed-phase precipitation in the melting layer at the PR frequency, including the effects of sensor response. These differences are plotted as functions of the radar reflectivity at the base of the melting layer, here assumed to be 1.5 km below the level of maximum reflectivity. Note that the FS snow/MGwi graupel model leads to significant increases in melting layer optical depths which increase with basal reflectivity (Fig. 10a). The maximum increase in the optical depth due to mixed-phase precipitation is 0.46 (-2 dB). The layer-mean reflectivities also increase with the introduction of mixed-phase precipitation, but the increase doesn't show a discernable trend with basal reflectivity (Fig. 10c). Maximum increases in the layer-mean reflectivities are on the order of 5 dBZ.

The FS snow/ML97 graupel model also yields increases in melting layer optical depths and mean reflectivities, but the magnitudes of these increases are generally reduced. Since attenuation in the melting layers is typically less, increases in layer-mean reflectivities can still be as large as 5 dBZ, although most increases are less than 2 dBZ.

6. Summary and Conclusions

The one-dimensional, steady-state melting layer model developed in Part I of this study is used to calculate both the microphysical and radiative properties of melting precipitation, based upon the computed concentrations of snow and graupel just above the freezing level at applicable horizontal gridpoints of 3-D CRM simulations. The modified 3-D distributions of hydrometeor properties serve as input to radiative transfer calculations of upwelling radiances and radar extinction/reflectivities at the TMI and PR frequencies, respectively. TMI-measured radiances and PR-measured extinction/reflectivities are then simulated, based upon the angular response characteristics of the two instruments.

At the resolution of the CRM grid (~1 km), upwelling radiances generally increase if mixed-phase, melting precipitation is included in the model atmosphere. The magnitude of the increase depends upon the total optical thickness of the cloud and precipitation, as well as the scattering characteristics of ice-phase precipitation aloft. At 10.65 and 19.35 GHz the optical thickness of cloud and precipitation is generally low, and so the additional absorption/emission by melting precipitation leads to a substantial increase in upwelling radiances. Over the set of CRM model simulations utilized in this study, maximum radiance increases of 43 K and 28 K are obtained at 10.65 and 19.35 GHz, respectively, using idealized models to represent the dielectric properties of the melting snow and graupel particles. At 37 GHz, the greater optical depths of precipitation lead to smaller increases (maximum of 18 K over all simulations) and sometimes decreases of upwelling radiances with the inclusion of mixed-phase precipitation. This trend continues at 85.5 GHz, but in addition, scattering by overlying ice-phase precipitation tends to damp the radiative effects of the melting layer. A maximum 85.5 GHz radiance increase of 10 K due to melting is produced by the set of CRM simulations, but increases less than 4 K are more typical.

The impact of melting on *TMI-measured* radiances is determined not only by the physics of the melting particles but also by the spatial extent of the melting precipitation, since the lower-frequency TMI channels have footprints which extend over 10's of kilometers. When sensor resolution is considered, the maximum radiance increases due to mixed-phase precipitation are reduced to 37%, 54%, 67%, and 90% of the grid-resolution values at 10.65, 19.35, 37, and 85.5 GHz, respectively.

Simulated PR extinction and reflectivities in the melting layer can increase dramatically if mixed-phase precipitation is included, a result consistent with previous studies; e.g. Meneghini and Liao (1996). The additional extinction by mixed-phase particles tends to increase as a function of the reflectivity below the melting layer, and a maximum increase of 0.46 (-2 dB) in extinction optical depth is simulated based upon the set of CRM simulations. The increase of the layer-mean reflectivity due to melting precipitation can be as much as 5 dBZ.

Parts I and II of this study lay the groundwork for more realistic radiance and reflectivity computations based upon CRM simulations. The next phase of this study will be to incorporate these cloud/radiative model simulations into methods for estimating precipitation and latent heating distributions using TMI, PR, or combined TMI and PR observations. As mentioned in the Section 1, a Bayesian framework for directly estimating precipitation and latent heating profiles using cloud/radiative model simulations has been developed by the authors. This method will be exploited to determine the sensitivity of precipitation/latent heating estimates to the physical parameterization of melting in the supporting model simulations.

Acknowledgments

The authors would like to thank Nicolas Viltard, Brad Ferrier, Daniel Johnson, Robert Meneghini, and Liang Liao for their helpful suggestions throughout the development of this work. The study was funded by the TRMM Science program.

References

Bauer, P., L. Schanz, and L. Roberti, 1998: Correction of three-dimensional effects for passive microwave remote sensing of convective clouds. *J. Appl. Meteor.*, **37**, 1619-1632.

Bauer, P., J. P. V. Poiares Baptista, and M. Iulis, 1999a: On the effect of the melting layer on microwave emission of clouds over the ocean. *J. Atmos. Sci.*, **56**, 852-867.

Bauer, P., A. Khain, I. Sednev, R. Meneghini, C. Kummerow, F. Marzano, and J. P. V. Poaires Baptista, 1999b: Combined cloud-microwave radiative transfer modeling of stratiform rainfall. Submitted to *J. Atmos. Sci.*

Heymsfield, A. J., and C. M. R. Platt, 1984: A parameterization of the particle size spectrum of ice clouds in terms of the ambient temperature and the ice water content. *J. Atmos. Sci.*, **41**, 846-855.

Liebe, H. J., 1985: An updated model for millimeter wave propagation in moist air, *Radio Sci.*, **20**, 1069-1089.

Liou, K-N., 1992: *Radiation and Cloud Processes in the Atmosphere: Theory, Observation and Modeling*. Oxford University Press, 487 pp.

Maxwell-Garnett, J. C., 1904: Colors in metal glasses and in metallic films. *Philos. Trans. Roy. Soc. London Ser. A*, **203**, 385-420.

Meneghini, R., and L. Liao, 1996: Comparisons for cross sections for melting hydrometeors as derived from dielectric mixing formulas and a numerical method. *J. Appl. Meteor.*, **35**, 1658-1670.

Mie, G., 1908: Beitrage zur optik truber median, speziell kolloidaler metallosungen. *Ann. Physik*, **25**, 377-445.

Olson, W. S., and C. D. Kummerow, 1996: Simulated retrieval of precipitation profiles from TRMM microwave imager and precipitation radar data. Preprints, *Eighth Conf. on Satellite Meteorology and Oceanography*, Atlanta, GA, Amer. Meteor. Soc., 248-251.

Olson, W. S., C. D. Kummerow, G. M. Heymsfield, and L. Giglio, 1996: A method for combined passive-active microwave retrievals of cloud and precipitation profiles. *J. Appl. Meteor.*, **35**, 1763-1789.

Petty, G. W., 1994: Physical retrievals of over-ocean rain rate from the multichannel microwave imagery. Part I: Theoretical characteristics of normalized polarization and scattering indices. *Meteorol. Atmos. Phys.*, **54**, 79-99.

Rickenbach, T. M., and S. A. Rutledge, 1998:" Convection in TOGA COARE: Horizontal scale, morphology, and rainfall production. *J. Atmos. Sci.*, **55**, 2715-2729.

Roberti, L., J. Haferman, and C. Kummerow, 1994: Microwave radiative transfer through horizontally inhomogeneous precipitating clouds. *J. Geophys. Res.*, **99**, 16707-16718.

Robinson, W., C. Kummerow, and W. S. Olson, 1992: A technique for matching the resolution of microwave measurements from the SSM/I instrument. *IEEE Trans. Geosci. Remote Sensing*, **30**, 419-429.

Schols, J., J. Haferman, J. Weinman, C. Prabhakara, M. Cadeddu, and C. Kummerow, 1997: Polarized microwave radiation model of melting deformed hydrometeors. Preprints, *Ninth Conf. on Atmospheric Radiation*, Long Beach, CA, Amer. Meteor. Soc., 270-273.

Weinman, J. A., and R. Davies, 1978: Thermal microwave radiances from horizontally finite clouds of hydrometeors. *J. Geophys. Res.*, **83**, 3099-3107.

Wilheit, T. T., 1979: A model for the microwave emissivity of the ocean's surface as a function of wind speed. *IEEE Trans. Geosci. Electron.*, **GE-17**, 244-249.

Tables

Table 1. Characteristics of the Tropical Rainfall Measuring Mission Microwave Imager and Precipitation Radar. The horizontal resolution specifications of the Precipitation Radar are at nadir view.

TRMM Microwave Imager (TMI)

Channel Frequency (GHz)	Half-power Beamwidth (deg.)	Horizontal Resolution (km)	Noise (K)
10.65	3.7	37 x 63	0.6
19.35	1.9	18 x 30	0.5
21.3	1.7	18 x 23	0.7
37.0	1.0	9 x 16	0.3
85.5	0.43	5 x 7	0.7

Precipitation Radar (PR)

Channel Frequency (GHz)	Half-power Beamwidth (deg.)	Horiz. Resolution at Surface / Range Resolution (km)	Uncertainty Due to Sampling (dB)
13.8	0.71	4.3 / 0.25	0.7

Figure Captions

Fig. 1. General schematic of the TMI and PR measurement geometry, relative to a 3-D CRM grid domain on the earth's surface.

Fig. 2. TOGA1 simulation of precipitation and radiance fields at 180 min of integration time. Panels (a) and (b) are plan views of vertically-integrated precipitating liquid and ice, respectively. Dotted line indicates the transect for the vertical cross sections shown in Figs. 6 and 7. Panels (c) and (d) are plan views of the grid-resolution, upwelling radiance fields at 19.35 and 85.5 GHz, respectively, computed using the slant-path Eddington (SPE) method. Panels (e) and (f) are the same as (c) and (d), but the radiances are computed using a reverse Monte Carlo (MC) method.

Fig. 3. Radiance differences between the slant-path Eddington (SPE) and the Monte Carlo (MC) methods at 5 km resolution, plotted as functions of the SPE radiances from the TOGA1, 180 min simulation. Plotted are radiance differences at (a) 10.65 GHz, (b) 19.35 GHz, (c) 37.0 GHz, and (d) 85.5 GHz.

Fig. 4. TOGA1 simulation of upwelling radiances at 180 min. integration time, including the effects of mixed-phase, melting precipitation. Panels are plan views of the grid-resolution, upwelling radiance fields at (a) 10.65 GHz, (b) 19.35 GHz, (c) 37.0 GHz, and (d) 85.5 GHz.

Fig. 5. Radiance difference fields between the TOGA1, 180 min. simulation including mixed-phase, melting precipitation and the same simulation without mixed-phase precipitation, both at model grid resolution. Positive differences indicate increased radiances due to the presence of mixed-phase precipitation. Plan views of the difference fields at (a) 10.65 GHz, (b) 19.35 GHz, (c) 37.0 GHz, and (d) 85.5 GHz are shown.

Fig. 6. Vertical cross sections at y = 75 km from the TOGA1, 180 min. simulation including mixed-phase, melting precipitation; see Fig. 2 for reference. Panels (a) and (b) show the vertical cross sections of precipitating liquid and ice, respectively. Simulated fields of 13.8 GHz extinction coefficient and radar reflectivity at model grid resolution are shown in panels (c) and (d), respectively. Exinction coefficient and radar reflectivity differences from simulations with and without mixed-phase precipitation are shown in panels (e) and (f), respectively.

Fig. 7. Radiance, extinction coefficient, and radar reflectivity difference fields from the TOGA1, 180 min. simulation, including sensor resolution effects. Shown in panels (a), (b), (c), and (d) are the upwelling radiance differences from simulations with and without mixed-phase melting precipitation at 10.65, 19.35, 37.0, and 85.5 GHz, respectively. Panels (e) and (f) are vertical cross sections at y = 75 km of the 13.8 GHz extinction

coefficient and radar reflectivity differences, respectively, from simulations with and without mixed-phase precipitation; see Fig. 2 for reference.

Fig. 8. Radiance differences at model grid resolution, from simulations with and without mixed-phase, melting precipitation, plotted as functions of the difference between effective atmospheric temperature (assumed to be 273 K) and the upwelling radiances simulated without mixed-phase precipitation. Plots in the left column are based on simulations that employ the Fabry-Szyrmer core-shell dielectric model for snow and the Maxwell-Garnett water matrix dielectric model for graupel. Plots in the right column are based on simulations that incorporate the Fabry-Szyrmer core-shell dielectric model for snow and the Meneghini and Liao (1997) dielectric model for graupel. Overlaid isolines of melting layer optical depth are based upon a simple, absorbing atmosphere model for upwelling radiance; see text for description.

Fig. 9. Same as Fig. 8, but radiance calculations include sensor resolution effects.

Fig. 10. Melting layer extinction optical depth and mean radar reflectivity differences at sensor resolution, from CRM simulations with and without mixed-phase, melting precipitation, plotted as functions of the radar reflectivity just below the melting layer. Plots (a) and (c) in the left column are based on simulations that employ the Fabry-

Szyrmer core-shell dielectric model for snow and the Maxwell-Garnett water matrix dielectric model for graupel. Plots (b) and (d) in the right column are based on simulations that incorporate the Fabry-Szyrmer core-shell dielectric model for snow and the Meneghini and Liao (1997) dielectric model for graupel.

Fig. 1

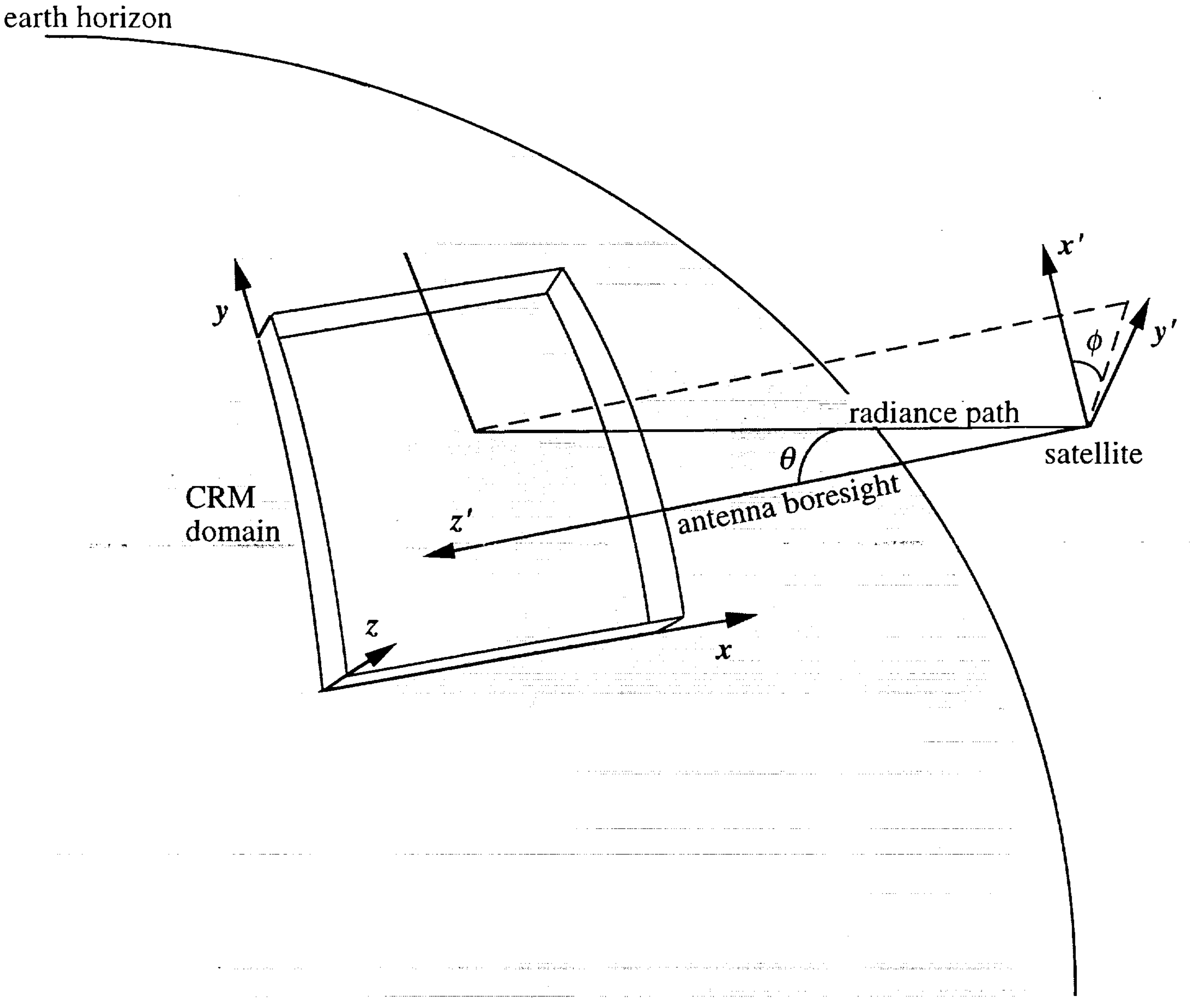
earth horizon
x'
y
y'
ϕ
radiance path
satellite
θ
CRM
domain
antenna boresight
z'
z
x

Fig. 2

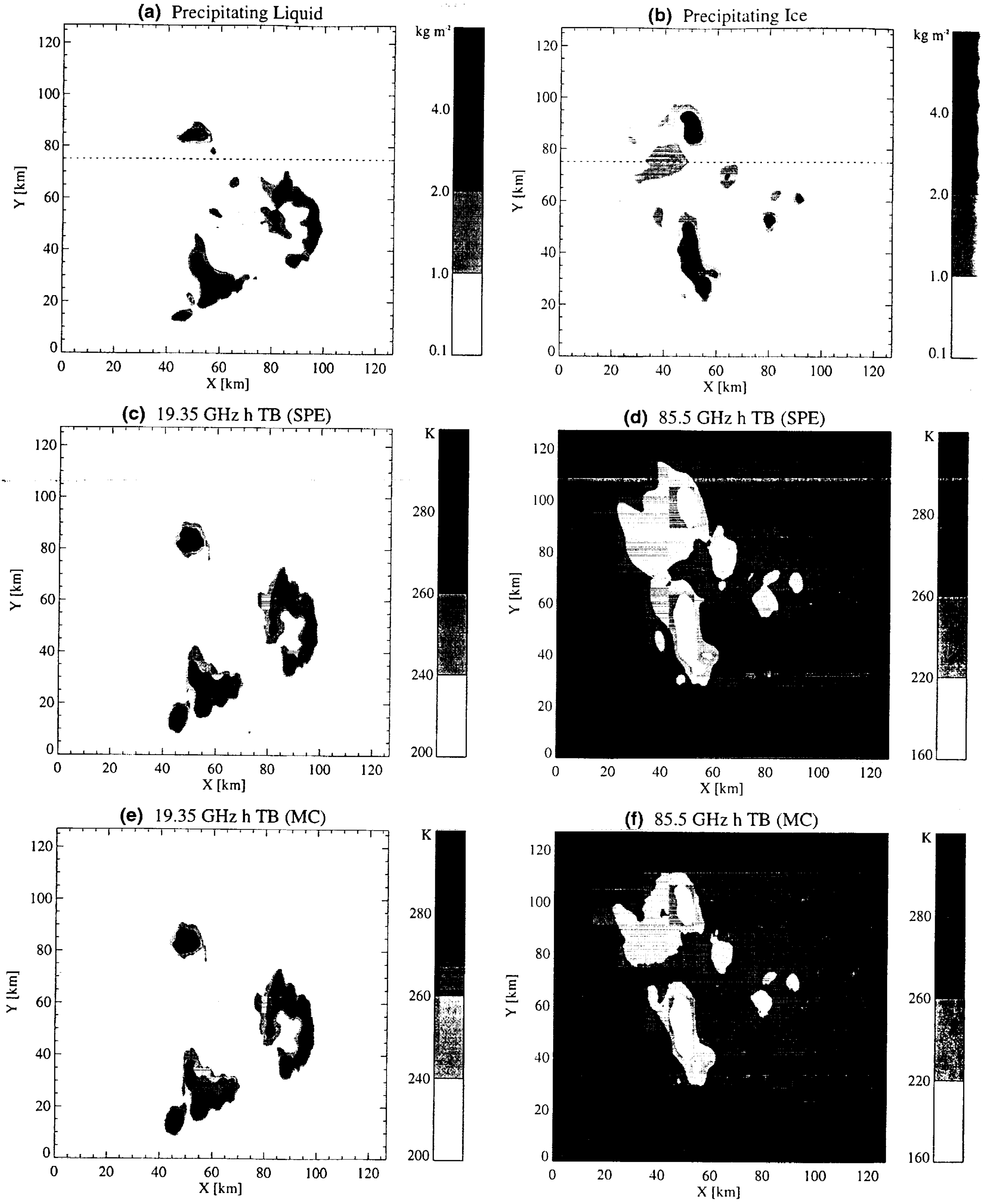
(a) Precipitating Liquid

(b) Precipitating Ice

(c) 19.35 GHz h TB (SPE)

(d) 85.5 GHz h TB (SPE)

(e) 19.35 GHz h TB (MC)

(f) 85.5 GHz h TB (MC)

Fig. 3

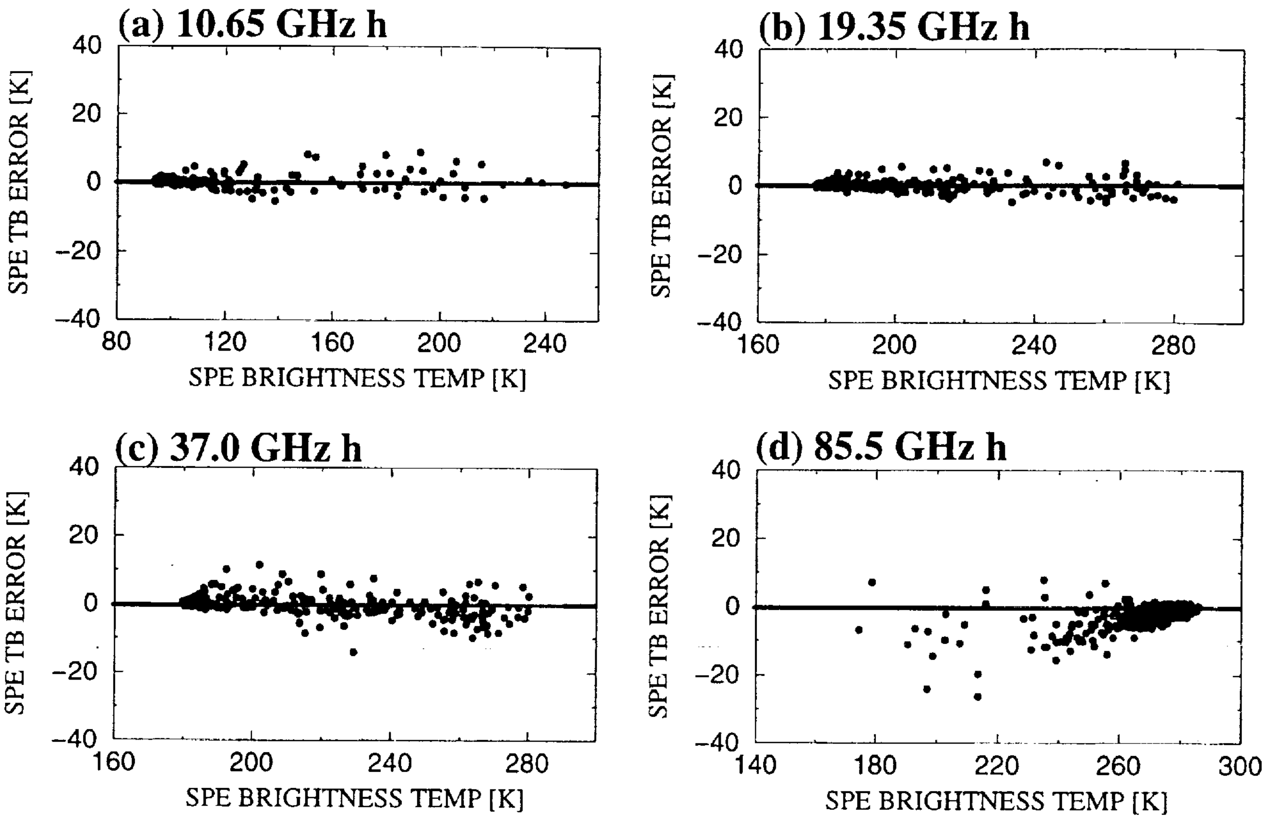

(a) 10.65 GHz h

(b) 19.35 GHz h

(c) 37.0 GHz h

(d) 85.5 GHz h

Fig. 4

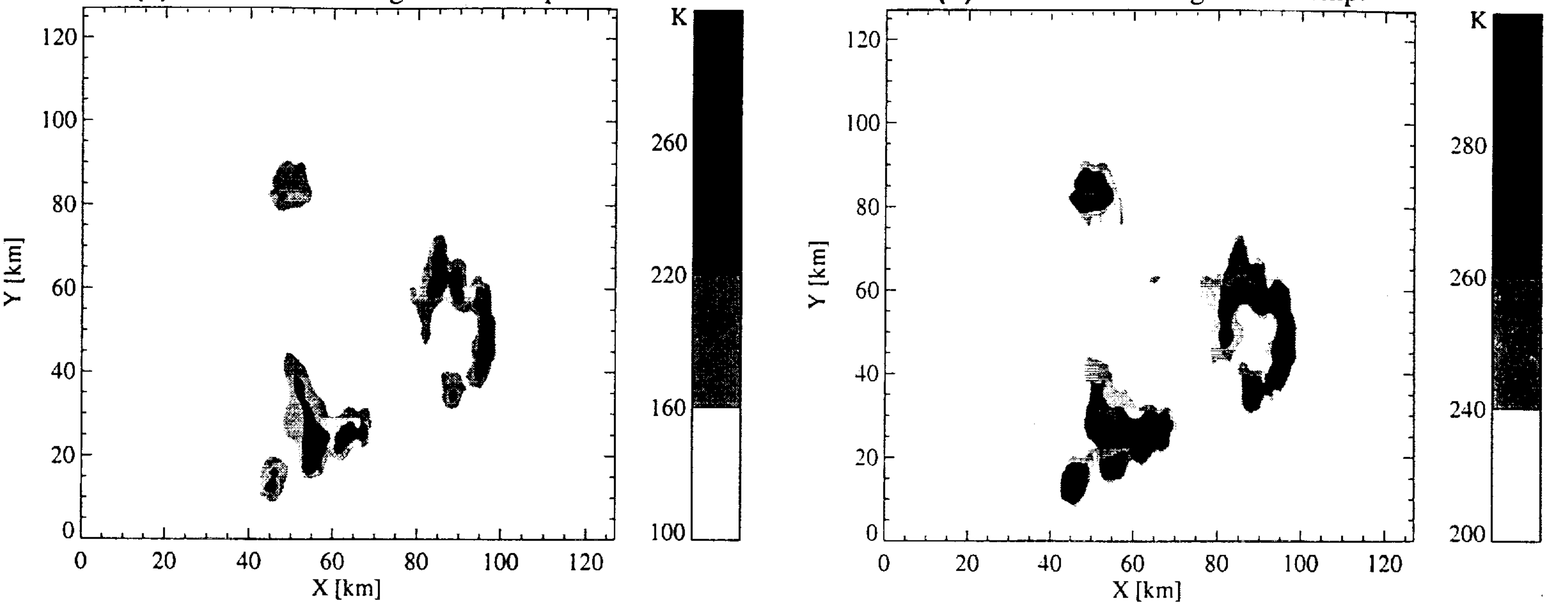

(a) 10.65 GHz h Brightness Temp.

(b) 19.35 GHz h Brightness Temp.

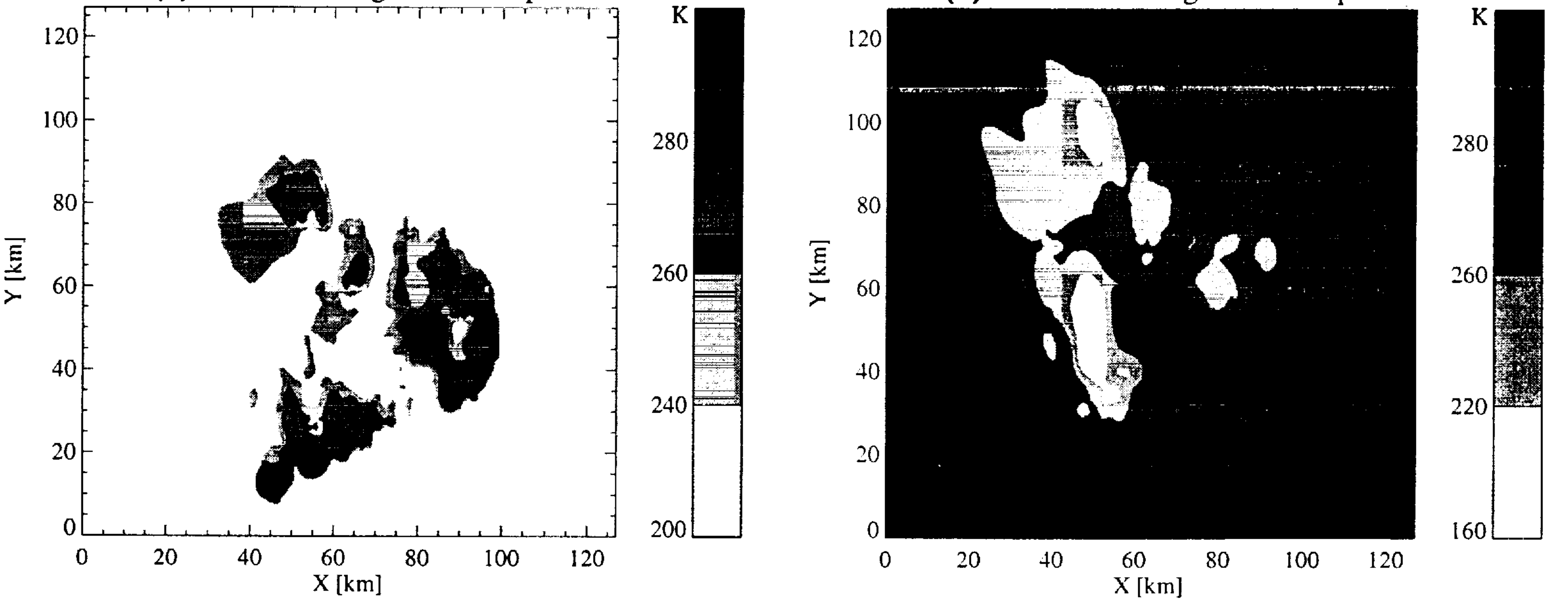

(c) 37 GHz h Brightness Temp.

(d) 85.5 GHz h Brightness Temp.

Fig. 5

(a) 10.65 GHz h TB Difference

(b) 19.35 GHz h TB Difference

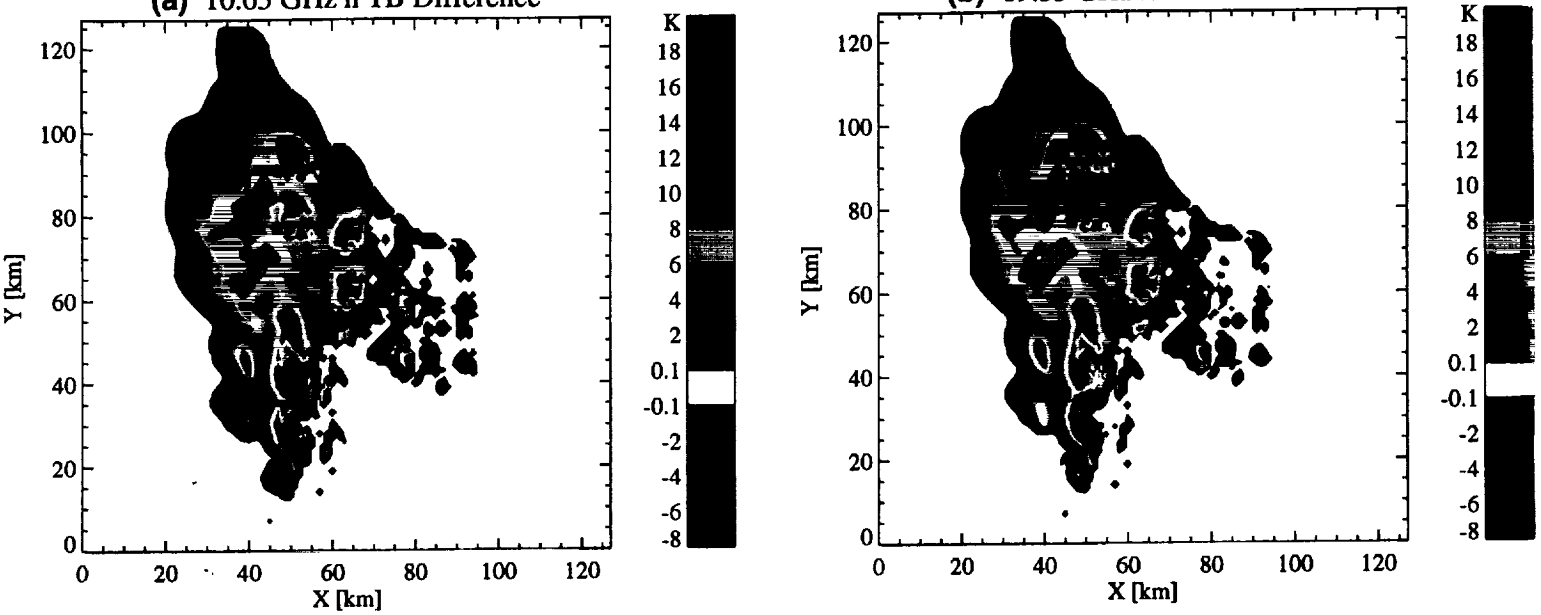

(c) 37 GHz h TB Difference

(d) 85.5 GHz h TB Difference

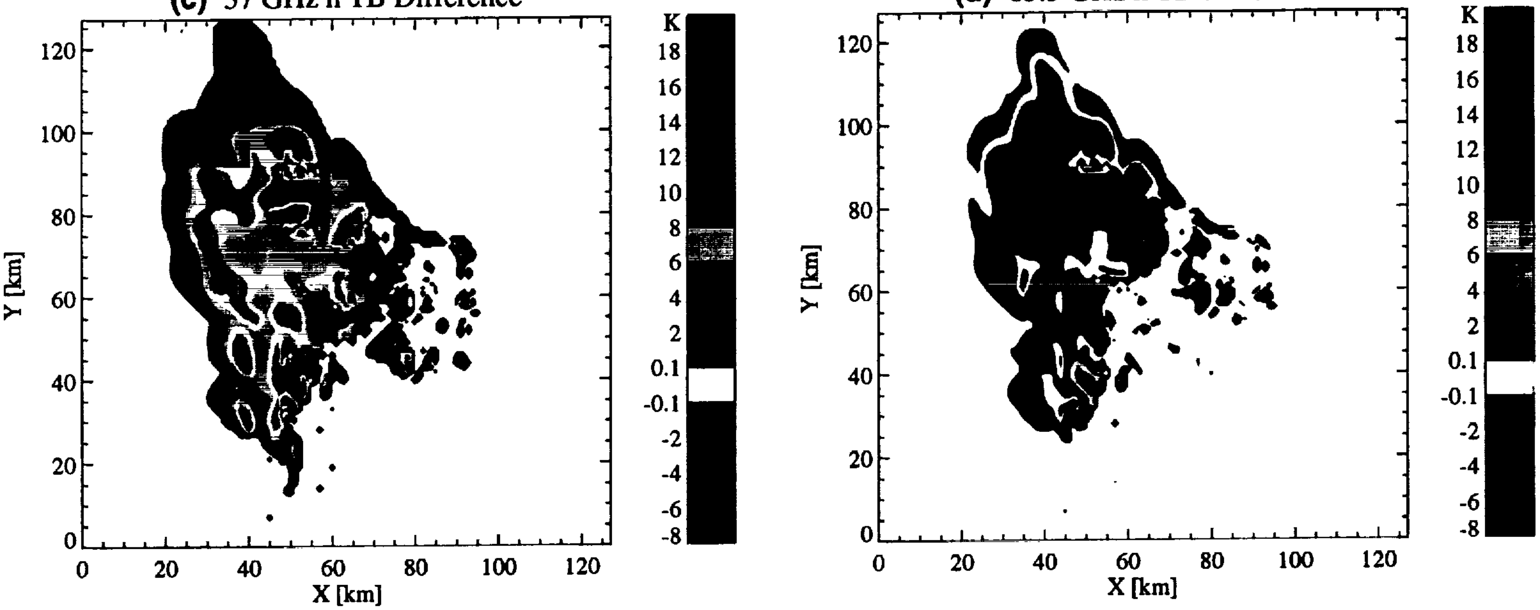

Fig. 6

(a) Precipitating Liquid **(b)** Precipitating Ice

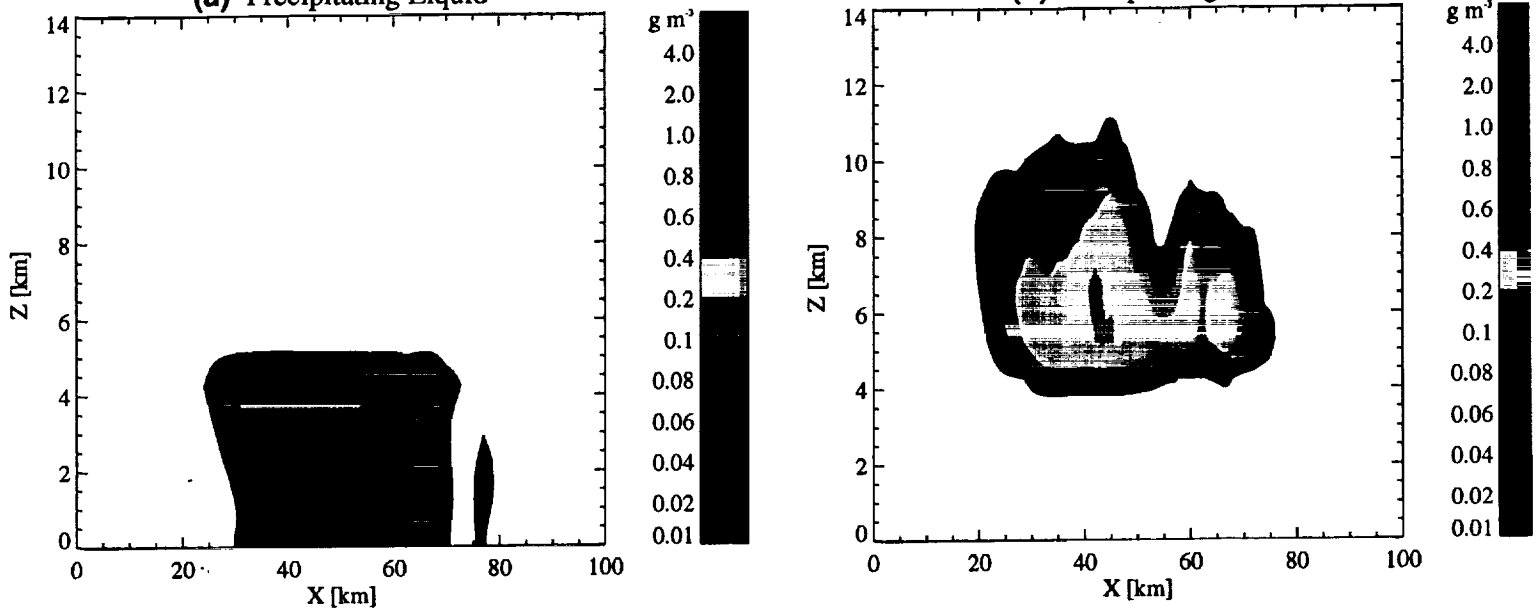

(c) 13.8 GHz Extinction **(d)** 13.8 GHz Reflectivity

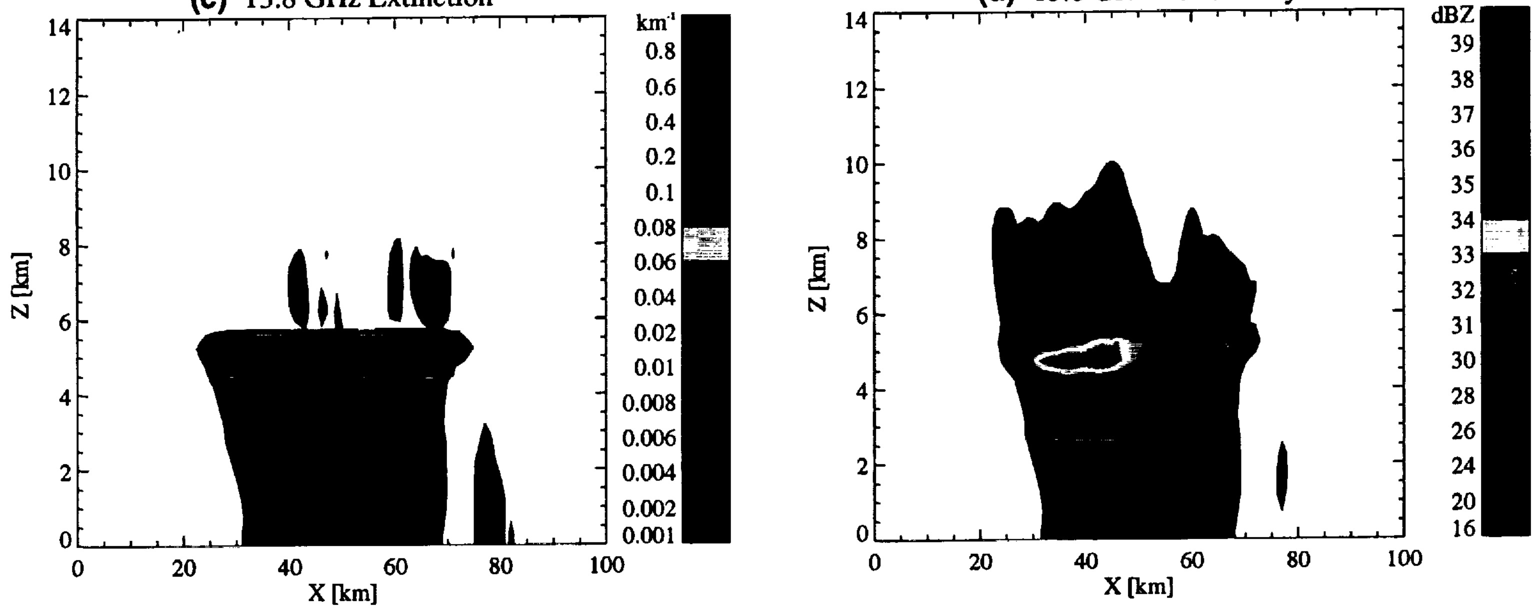

(e) 13.8 GHz Ext. Difference **(f)** 13.8 GHz Refl. Difference

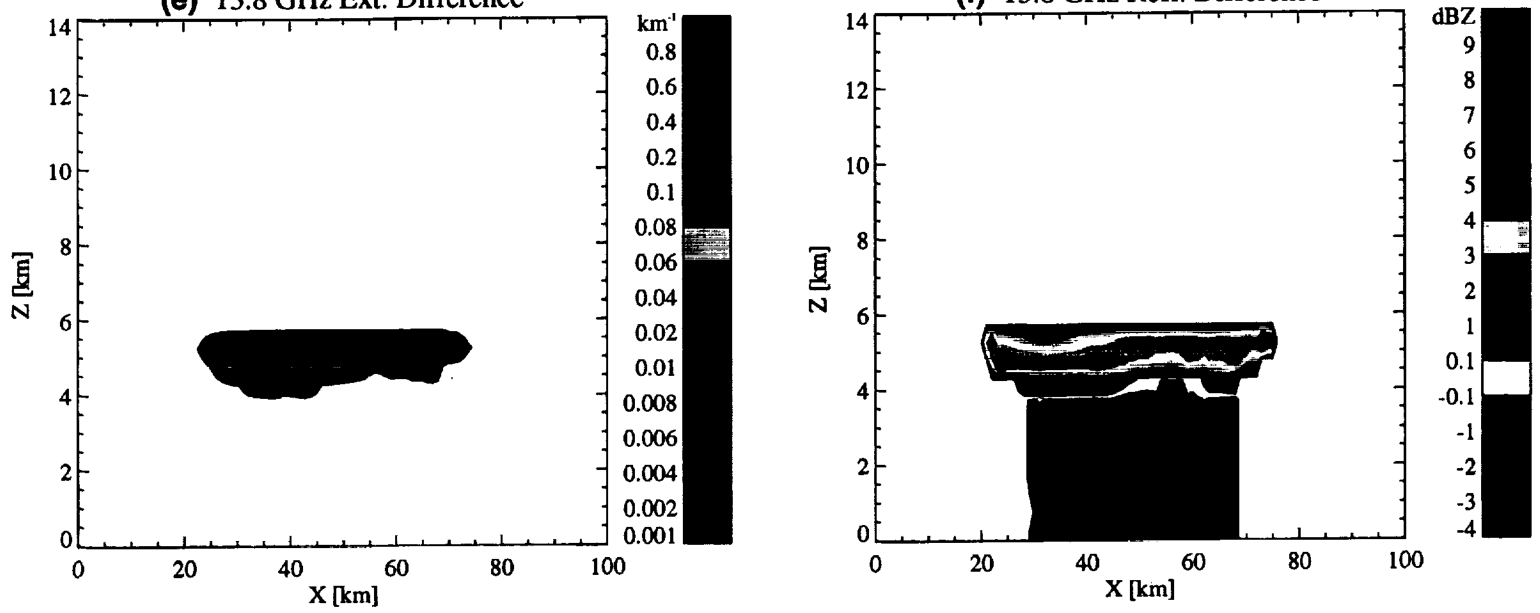

Fig. 7

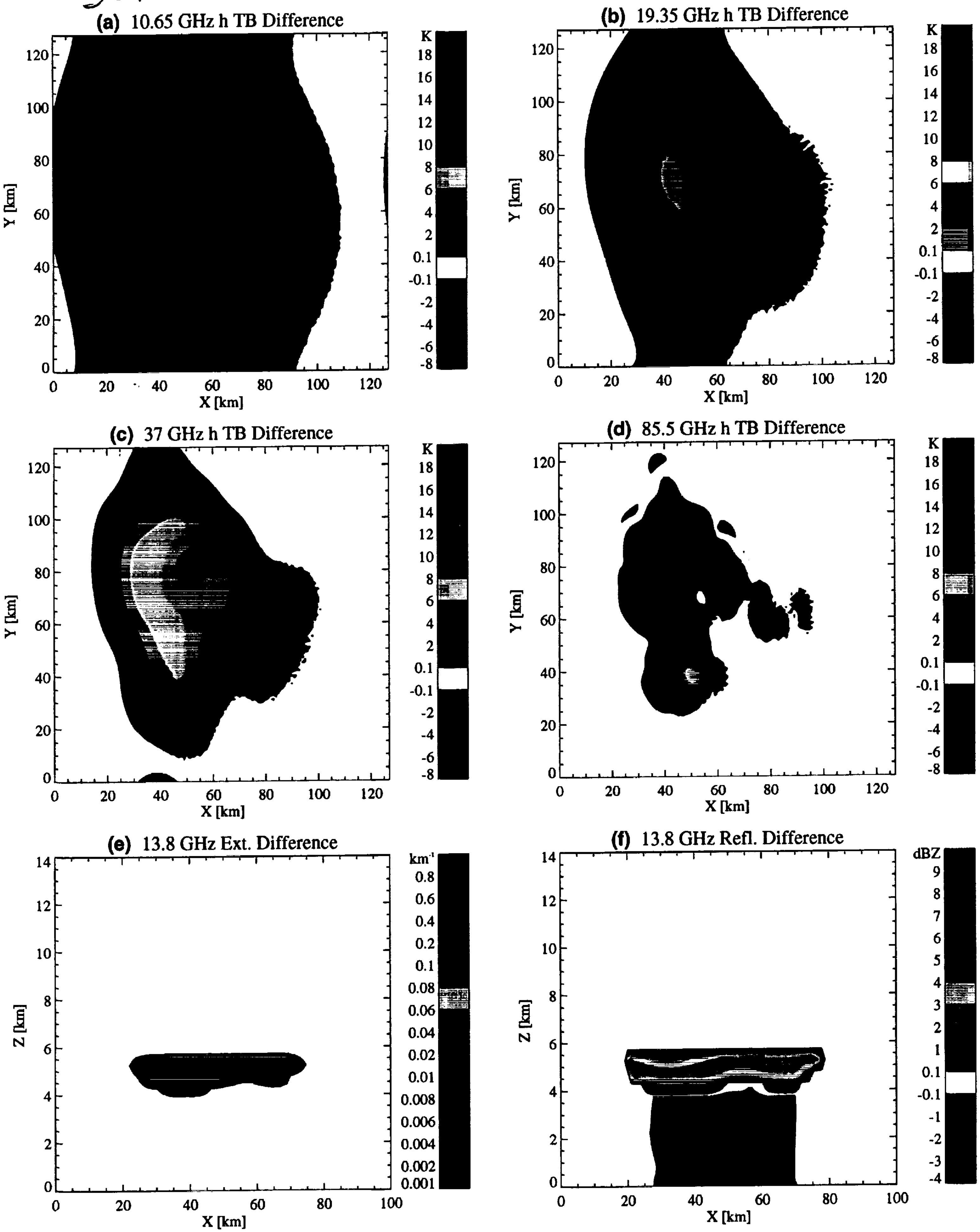

(a) 10.65 GHz h TB Difference

(b) 19.35 GHz h TB Difference

(c) 37 GHz h TB Difference

(d) 85.5 GHz h TB Difference

(e) 13.8 GHz Ext. Difference

(f) 13.8 GHz Refl. Difference

Fig. 8

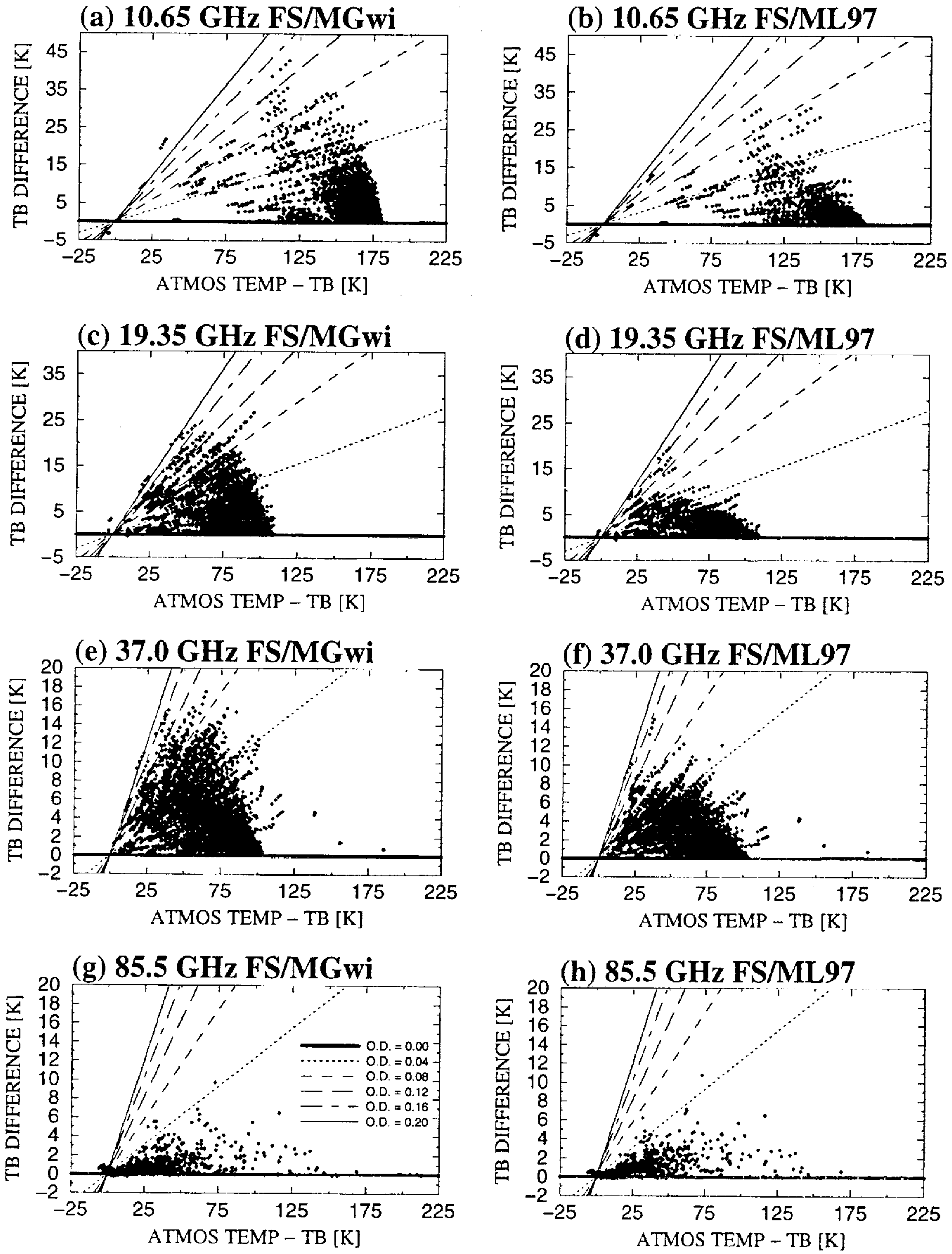
(a) 10.65 GHz FS/MGwi
(b) 10.65 GHz FS/ML97
(c) 19.35 GHz FS/MGwi
(d) 19.35 GHz FS/ML97
(e) 37.0 GHz FS/MGwi
(f) 37.0 GHz FS/ML97
(g) 85.5 GHz FS/MGwi
(h) 85.5 GHz FS/ML97
TB DIFFERENCE [K]
ATMOS TEMP – TB [K]
−25
25
75
125
175
225
−5
5
15
25
35
45
−2
0
2
4
6
8
10
12
14
16
18
20
O.D. = 0.00
O.D. = 0.04
O.D. = 0.08
O.D. = 0.12
O.D. = 0.16
O.D. = 0.20

Fig. 9

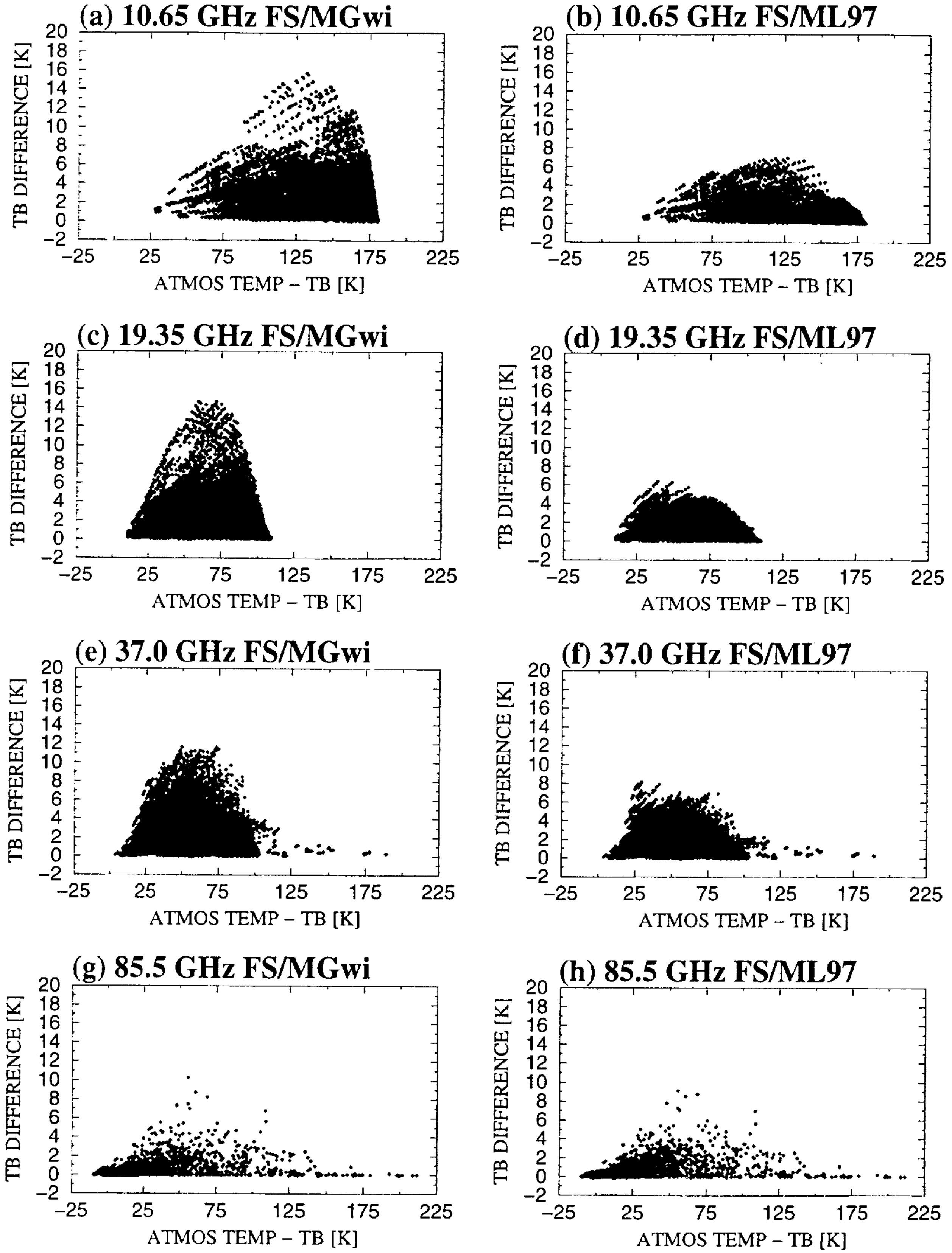
(a) 10.65 GHz FS/MGwi
(b) 10.65 GHz FS/ML97
(c) 19.35 GHz FS/MGwi
(d) 19.35 GHz FS/ML97
(e) 37.0 GHz FS/MGwi
(f) 37.0 GHz FS/ML97
(g) 85.5 GHz FS/MGwi
(h) 85.5 GHz FS/ML97
TB DIFFERENCE [K]
-2
0
2
4
6
8
10
12
14
16
18
20
ATMOS TEMP – TB [K]
-25
25
75
125
175
225

Fig. 10

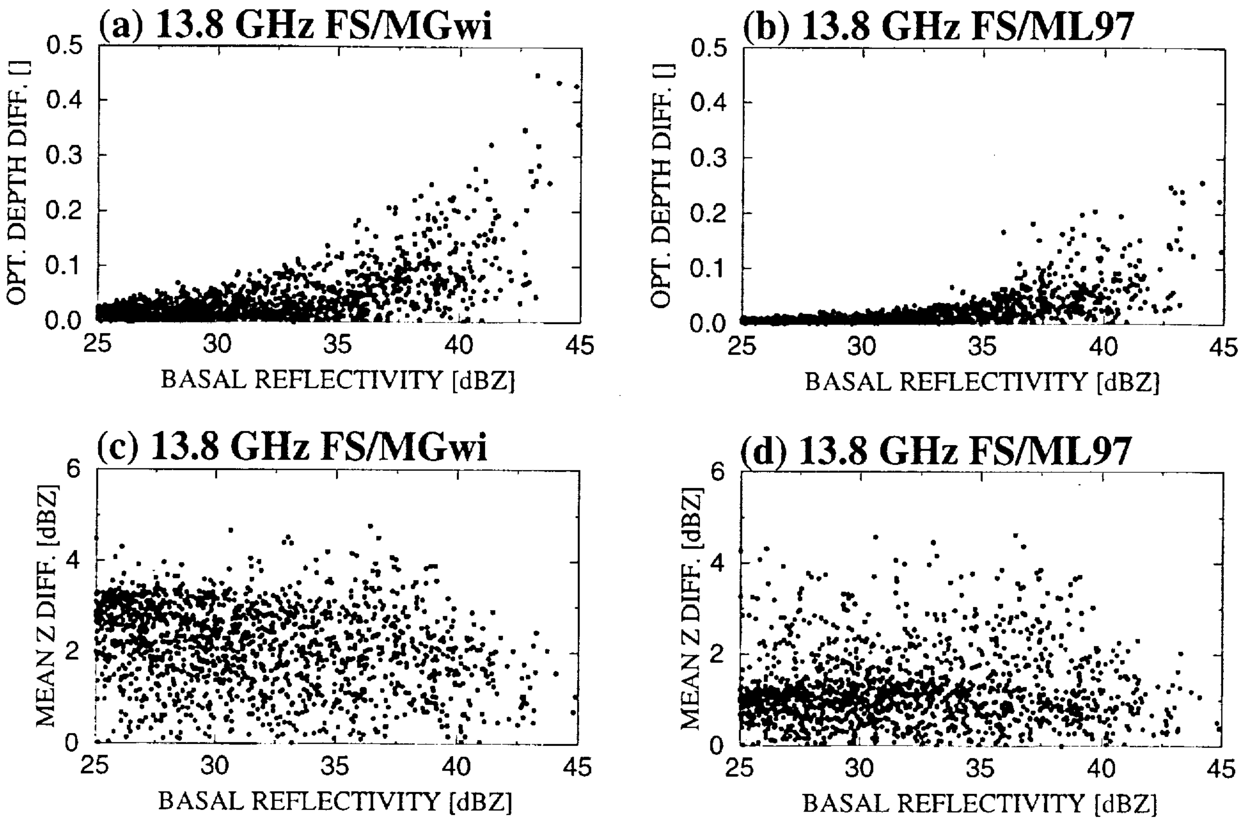
(a) 13.8 GHz FS/MGwi
OPT. DEPTH DIFF. []
0.0
0.1
0.2
0.3
0.4
0.5
25
30
35
40
45
BASAL REFLECTIVITY [dBZ]
(b) 13.8 GHz FS/ML97
OPT. DEPTH DIFF. []
0.0
0.1
0.2
0.3
0.4
0.5
25
30
35
40
45
BASAL REFLECTIVITY [dBZ]
(c) 13.8 GHz FS/MGwi
MEAN Z DIFF. [dBZ]
0
2
4
6
25
30
35
40
45
BASAL REFLECTIVITY [dBZ]
(d) 13.8 GHz FS/ML97
MEAN Z DIFF. [dBZ]
0
2
4
6
25
30
35
40
45
BASAL REFLECTIVITY [dBZ]